

IUTAM Bookseries

Stefanie Gutschmidt  
James N. Hewett  
Mathieu Sellier *Editors*

# **IUTAM** Symposium on Recent Advances in Moving Boundary Problems in Mechanics

Proceedings of the IUTAM Symposium  
on Moving Boundary Problems,  
Christchurch, New Zealand,  
February 12–15, 2018

 Springer

# **IUTAM Bookseries**

Volume 34

The IUTAM Bookseries publishes the refereed proceedings of symposia organized by the International Union of Theoretical and Applied Mechanics (IUTAM).

Every two years the IUTAM General Assembly decides on the list of IUTAM Symposia. The Assembly calls upon the advice of the Symposia panels. Proposals for Symposia are made through the Assembly members, the Adhering Organizations, and the Affiliated Organizations, and are submitted online when a call is launched on the IUTAM website.

The IUTAM Symposia are reserved to invited participants. Those wishing to participate in an IUTAM Symposium are therefore advised to contact the Chairman of the Scientific Committee in due time in advance of the meeting. From 1996 to 2010, Kluwer Academic Publishers, now Springer, was the preferred publisher of the refereed proceedings of the IUTAM Symposia. Proceedings have also been published as special issues of appropriate journals. From 2018, this bookseries is again recommended by IUTAM for publication of Symposia proceedings.

Indexed in Ei Compendex and Scopus.

More information about this series at <http://www.springer.com/series/7695>

Stefanie Gutschmidt · James N. Hewett ·  
Mathieu Sellier  
Editors

# IUTAM Symposium on Recent Advances in Moving Boundary Problems in Mechanics

Proceedings of the IUTAM Symposium  
on Moving Boundary Problems, Christchurch,  
New Zealand, February 12–15, 2018

 Springer

*Editors*

Stefanie Gutschmidt  
Department of Mechanical Engineering  
University of Canterbury  
Christchurch, New Zealand

James N. Hewett  
Department of Mechanical Engineering  
University of Canterbury  
Christchurch, New Zealand

Mathieu Sellier  
Department of Mechanical Engineering  
University of Canterbury  
Christchurch, New Zealand

ISSN 1875-3507

ISSN 1875-3493 (electronic)

IUTAM Bookseries

ISBN 978-3-030-13719-9

ISBN 978-3-030-13720-5 (eBook)

<https://doi.org/10.1007/978-3-030-13720-5>

Library of Congress Control Number: 2019931856

© Springer Nature Switzerland AG 2019

This work is subject to copyright. All rights are reserved by the Publisher, whether the whole or part of the material is concerned, specifically the rights of translation, reprinting, reuse of illustrations, recitation, broadcasting, reproduction on microfilms or in any other physical way, and transmission or information storage and retrieval, electronic adaptation, computer software, or by similar or dissimilar methodology now known or hereafter developed.

The use of general descriptive names, registered names, trademarks, service marks, etc. in this publication does not imply, even in the absence of a specific statement, that such names are exempt from the relevant protective laws and regulations and therefore free for general use.

The publisher, the authors and the editors are safe to assume that the advice and information in this book are believed to be true and accurate at the date of publication. Neither the publisher nor the authors or the editors give a warranty, express or implied, with respect to the material contained herein or for any errors or omissions that may have been made. The publisher remains neutral with regard to jurisdictional claims in published maps and institutional affiliations.

This Springer imprint is published by the registered company Springer Nature Switzerland AG  
The registered company address is: Gewerbestrasse 11, 6330 Cham, Switzerland

# Preface

## Background

Many problems in mechanics involve a deformable domain with moving boundaries. Examples include two-way fluid–structure interaction, free surface flows, flows over soft tissues and textiles, flows involving accretion/erosion, flows through deformable porous media, material forming, to name but a few. The interaction of the moving boundary with the participating medium leads to fascinating phenomena in a very broad range of contexts such as flutter, wave breaking, dune formation, ripple formation on the ocean floor, flow instabilities, structure resonance and failure, atherosclerosis, ice formation on aircraft wings, etc.

The presence of a moving boundary also presents considerable challenges when it comes to modeling and understanding the underlying system dynamics. The moving boundary often introduces nonlinearities, which call for special analytical or numerical treatment. Many techniques have been developed over the years to handle the moving boundary and the corresponding deformable medium. Examples include front tracking methods, front fixing methods, the volume of fluid method, the arbitrary Lagrangian–Eulerian method, etc. These methods have allowed the community to tackle forever more complex problems of engineering and physics, but challenges still remain and the range of applications for which these techniques can be applied is vast.

## Symposium

The IUTAM symposium on “Recent Advances in Moving Boundary Problems in Mechanics” occurred from February 12 to February 15, 2018 in Christchurch, New Zealand. The aims of the symposium were to

1. gather the international community of engineers and scientists involved in moving boundary problems in mechanics,
2. attract a broad spectrum of researchers from various backgrounds (theoreticians, numerical analysts, experimentalists, applied mathematicians, engineers, physicists, etc.), and
3. unify a fragmented community to cross-fertilize ideas.

It was a pleasure to host about 50 participants from 17 different countries, a truly international cross section of the field. The single stream format of the symposium over 4 days afforded many opportunities for all participants to interact and get to know one another. Talks were broadly organized in themes: fluid–structure interaction, bioengineering applications, multiphase flows, analytical and numerical methods, Stefan problems, structures with a moving boundary, and optimization. The symposium had a good mix of participants (65% Engineering, 31% Applied Mathematics, 4% Physics). Presentations also spanned the whole spectrum from theory to applications. Most of the talks were oriented toward fluid mechanics (approximately 40% fluid, 40% fluid–structure interaction, 20% solid).

We were delighted to have had four engaging and inspiring plenary talks:

1. Prof. Yvonne Stokes (University of Adelaide): “Can we fabricate that fibre?”
2. Prof. Scott McCue (Queensland University of Technology): “Three dimensional linear and nonlinear surface wave patterns”
3. Prof. Jun Zhang (NYU): “Symmetry breaking bifurcations arising from fluid-structure interaction”
4. Prof. Frederic Dias (University College Dublin): “Recent advances in slamming”

We gratefully acknowledge their contribution to the success of the symposium.

Beyond the stimulating environment of the symposium, we will also keep fond memories of the social events including the symposium banquet and the Akaroa Harbour cruise.

Finally, we would like to acknowledge the professional and financial support of IUTAM, the College of Engineering at the University of Canterbury, the scientific committee, and local organizing team. Our special and personal thanks go to the symposium secretary James N. Hewett, who ran this symposium in such a way that everyone will keep this symposium in mind with very pleasant memories.



In summary, this symposium not only “moved boundaries” but also broke boundaries between researchers and pushed them to enhance knowledge in the field.

Christchurch, New Zealand

Stefanie Gutschmidt  
James N. Hewett  
Mathieu Sellier

# Contents

<b>1</b>	<b>Can We Fabricate That Fibre?</b> .....	<b>1</b>
	Yvonne M. Stokes, Darren G. Crowdy, Heike Ebendorff-Heidepriem, Peter Buchak and Michael J. Chen	
<b>2</b>	<b>A Numerical Study on Free Hovering Fruit-Fly with Flexible Wings</b> .....	<b>15</b>
	Y. Yao, K. S. Yeo and T. T. Nguyen	
<b>3</b>	<b>Three-Dimensional Flight Simulation with Transient Moving-Aerofoil Models</b> .....	<b>27</b>
	Arion Pons and Fehmi Cirak	
<b>4</b>	<b>Vortex Shedding and Flow-Induced Vibration of Two Cylinders in Tandem</b> .....	<b>41</b>
	Negar Hosseini, Martin D. Griffith and Justin S. Leontini	
<b>5</b>	<b>Flow-Induced Vibration and Energy Harvesting Using Fully-Passive Flapping Foils</b> .....	<b>53</b>
	Justin S. Leontini, Martin D. Griffith, David Lo Jacono and John Sheridan	
<b>6</b>	<b>Passive Cavitation Detection During Skin Sonoporation</b> .....	<b>63</b>
	Jeremy Robertson, Marie Squire and Sid Becker	
<b>7</b>	<b>CFD Reconstruction of Blood Hemodynamic Based on a Self-made Algorithm in Patients with Acute Type IIIb Aortic Dissection Treated with TEVAR Procedure</b> .....	<b>75</b>
	A. Polanczyk, A. Piechota-Polanczyk, Ch. Neumayer and I. Huk	
<b>8</b>	<b>The Three Dynamical Regimes of a Droplet Driven by Thermocapillarity</b> .....	<b>85</b>
	Jonatan Raúl Mac Intyre, Juan Manuel Gomba, Carlos Alberto Perazzo, Pablo Germán Correa and Mathieu Sellier	

<b>9</b>	<b>Simulation of the Ultrasound-Induced Growth and Collapse of a Near-Wall Bubble</b> . . . . .	97
	Bradley Boyd and Sid Becker	
<b>10</b>	<b>Air Flow Entrainment of Lactose Powder: Simulation and Experiment</b> . . . . .	107
	Thomas Kopsch, Darragh Murnane and Digby Symons	
<b>11</b>	<b>Oblique Impact of a Droplet on a Textured Substrate</b> . . . . .	119
	Hossein Rashidian and Mathieu Sellier	
<b>12</b>	<b>Numerical Simulation in Coupled Hydroelastic Problems by Using the LS-STAG Immersed Boundary Method</b> . . . . .	133
	Iliia K. Marchevsky and Valeria V. Puzikova	
<b>13</b>	<b>On the Efficiency of the Parallel Algorithms in VM2D Open Source Code for 2D Flows Simulation Using Vortex Methods</b> . . . . .	147
	Kseniia Kuzmina and Iliia K. Marchevsky	
<b>14</b>	<b>A Geometry-Adaptive Immersed Boundary–Lattice Boltzmann Method for Modelling Fluid–Structure Interaction Problems</b> . . . . .	161
	Lincheng Xu, Li Wang, Fang-Bao Tian, John Young and Joseph C. S. Lai	
<b>15</b>	<b>Toward the Problem of Low Re Flows Through Linearly Elastic Porous Media</b> . . . . .	173
	Sid Becker	
<b>16</b>	<b>Approximate Analytic Solution of the One Phase Stefan Problem for the Sphere</b> . . . . .	185
	R. B. Shorten	
<b>17</b>	<b>Selection Criterion of Stable Mode of Dendritic Growth with <math>n</math>-Fold Symmetry at Arbitrary Péclet Numbers with a Forced Convection</b> . . . . .	203
	Dmitri V. Alexandrov and Peter K. Galenko	
<b>18</b>	<b>Evolution of a Melting Sphere in Cross Flow Using an Arbitrary Mesh Topology</b> . . . . .	217
	James N. Hewett and Mathieu Sellier	
<b>19</b>	<b>Analysis of 3D Crack Boundary Problems by Means of the Enriched Scaled Boundary Finite Element Method</b> . . . . .	231
	Sascha Hell and Wilfried Becker	
<b>20</b>	<b>Analysis of Dynamic Variable Mass and Variable Parameter Systems Applying Semi-analytic Time-Integration</b> . . . . .	239
	Helmut J. Holl	

**21 Equipartition of Modal Energy in a Stiff Vibrating String  
Due to a Finite Curved Boundary Obstacle . . . . . 253**  
Ashok K. Mandal and Pankaj Wahi

**22 FEM with Floquet Theory for Non-slender Elastic Columns  
Subject to Harmonic Applied Axial Force Using 2D and  
3D Solid Elements . . . . . 267**  
Eoin Clerkin and Markus Rieken

**23 Effects of Non-neighbouring Members in an Array  
of Beams Vibrating in Fluids . . . . . 283**  
Arun Kumar Manickavasagam, Stefanie Gutschmidt  
and Mathieu Sellier

**Author Index . . . . . 295**

# Chapter 1

## Can We Fabricate That Fibre?



Yvonne M. Stokes, Darren G. Crowdy, Heike Ebendorff-Heidepriem,  
Peter Buchak and Michael J. Chen

**Abstract** This paper reviews the development of an efficient mathematical model for the drawing of optical fibres using extensional flow theory which is applicable for fibres of arbitrary geometry. The model is comprised of a 1D axial stretching problem describing the change in area of the cross-section from preform to fibre coupled with a 2D cross-plane problem describing the evolution of a cross-section. The solution of the axial stretching problem may be written in an exact form while the cross-plane problem must, in general, be solved numerically. The model may be used to solve forward and inverse problems and gives results that compare well with experiments.

**Keywords** Extensional flow · Free-boundary problem · Optical fibres

### 1.1 Introduction

Modelling of fibre drawing has been a topic of interest for around five decades, motivated initially by the ‘spinning’ of textile fibres [13] and film-blowing [14], and, more recently, by optical fibre technologies [1, 2, 5–8, 15–18] and the fabrication

---

Y. M. Stokes (✉) · M. J. Chen  
School of Mathematical Sciences, The University of Adelaide,  
Adelaide, SA 5005, Australia  
e-mail: [yvonne.stokes@adelaide.edu.au](mailto:yvonne.stokes@adelaide.edu.au)  
URL: <http://www.maths.adelaide.edu.au/yvonne.stokes/>

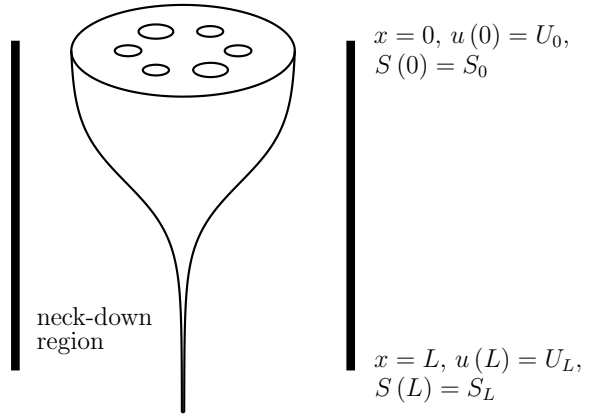
D. G. Crowdy  
Department of Mathematics, Imperial College London,  
London SW7 2AZ, UK

H. Ebendorff-Heidepriem  
Institute for Photonics and Advanced Sensing, School of Chemistry and Physics,  
The University of Adelaide, Adelaide, SA 5005, Australia

P. Buchak  
LowReTech LLC, 3401 Market St, Suite 200, Philadelphia, PA 19104, USA

© Springer Nature Switzerland AG 2019  
S. Gutschmidt et al. (eds.), *IUTAM Symposium on Recent Advances  
in Moving Boundary Problems in Mechanics*, IUTAM Bookseries 34,  
[https://doi.org/10.1007/978-3-030-13720-5\\_1](https://doi.org/10.1007/978-3-030-13720-5_1)

**Fig. 1.1** Schematic diagram of the neck-down region,  $0 \leq x \leq L$ , over which the cross-sectional area of the preform  $S_0$  reduces to that of the fibre  $S_L$  due to the large draw speed  $U_L$  relative to the feed speed  $U_0$ . © 2016 IEEE. Reprinted, with permission, from Chen et al., *J. Lightwave Tech.* 34(24), 5651–5656 (2016) [3, Fig. 1]



of capillary tubes [9]. The aim of this paper is to review key research in the context of drawing of microstructured optical fibres.

Microstructured optical fibres, containing patterns of air channels running along their length, have revolutionised optical fibre technology, promising a virtually limitless range of fibre designs for a wide range of applications, including communication networks, medical devices and sensing [10, 11]. These are fabricated as depicted in Fig. 1.1; a preform (1–3 cm diameter and with a length of around 10 cm or so), with a cross-section of appropriate geometry and having area  $S_0$ , is fed into a heated region at a feed speed  $U_0$  and pulled at a higher draw speed  $U_L$  by winding onto a spool some distance downstream beyond the neck-down region of length comparable to, but not necessarily identical with, the heated region. Internal channels may be pressurised. In the laboratory reference frame this drawing process over the neck-down region  $0 \leq x \leq L$  may be considered a steady-state problem. The resulting fibre will, typically, have a diameter of 100–200  $\mu\text{m}$ , a cross-sectional area  $S_L \ll S_0$ , and a length of a kilometre or more, while the internal air channels have diameters comparable to the wavelength of light. Even when the channels are not pressurised, the fibre drawing process modifies the shape of the cross-sectional geometry from that of the preform (see Fig. 1.2), as well as its scale, so that fabrication of a fibre with a desired structure presents a major challenge. What initial preform is suitable and what draw parameters should be used? Can it even be made? This is an inverse problem and mathematics is essential to its solution.

While full 3D numerical simulation has been used to investigate deformation of the cross-sectional geometry during fibre drawing [16, 17], this is still not practical for fibres with complex cross-sectional geometries because of the fine mesh resolution and large computational resources required. However, the slenderness of the geometry enables extensional flow theory to be used to develop accurate and efficient models and we here focus on these.

The first such model of steady-state fibre drawing seems to be due to Matovich and Pearson [13] who examined the drawing of solid axisymmetric fibres having no

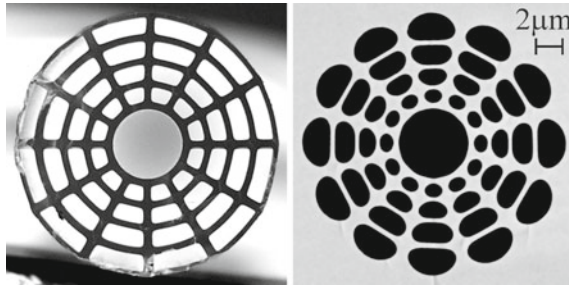


**Fig. 1.2** Cross-sectional geometry of (left) a fibre preform with total pattern diameter 3 cm, and (right) the resulting fibre with total pattern diameter  $20\ \mu\text{m}$ . These show the deformation due to the fibre drawing process. Photographs reproduced with the permission of the Institute for Photonics and Advanced Sensing, The University of Adelaide

internal structure. They obtained the form of the solution assuming a Newtonian fluid and neglecting surface tension and/or inertial forces; they also considered some non-Newtonian fluid models. Dewynne, Howell and Wilmott [7] showed that, assuming a Newtonian fluid and with neglect of surface tension, fibre drawing results only in a change in the cross-sectional scale, but not its shape, so that the steady-state model, for any given preform geometry, may be written as a boundary-value problem in one spatial dimension for the cross-sectional area as a function of axial position, which is readily solved. In an appendix they also noted that, for the case of non-negligible surface tension, the first-order model for the cross-sectional area is the same as for the zero surface tension case, but that the cross-section no longer maintains its shape which must be determined by solving a second-order 2D cross-flow problem. Modelling of fibre drawing including surface tension was considered in detail by Cummings and Howell [5] for fibres with no internal cross-sectional geometry and for a fluid of constant temperature (viscosity). They showed that the 2D cross-flow problem may be written as a classical 2D free-boundary Stokes-flow problem.

Motivated specifically by the drawing of microstructured optical fibres, Fitt et al. [8] used extensional-flow theory to derive coupled flow and temperature models for the steady drawing of axisymmetric capillary tubes. A Newtonian viscous fluid with temperature-dependent viscosity was assumed and inertia, gravity, surface tension and pressurisation of internal channels were included in the model. Various cases neglecting one or more of these were considered but the complete exact solution for isothermal fibre drawing with non-negligible surface tension, and neglecting inertia, gravity and pressurisation, was not found. Griffiths and Howell [9] obtained the solution for thin-walled annular tubes in their work extending the model of Cummings and Howell [5] to the non-isothermal drawing of (not necessarily axisymmetric) thin-walled tubes.

Solution of the extensional flow model with non-negligible surface tension for the drawing of microstructured optical fibres of arbitrary cross-sectional geometry and, indeed, also the drawing of an annular tube with arbitrary wall thickness, proved elusive but was finally solved by Stokes et al. [15]. The breakthrough that led to

this model is described in Sect. 1.2. Importantly, both forward and inverse problems may be solved as described in Sect. 1.3. Pressurisation of internal channels is not considered in this paper but was added by Chen et al. [2]. Section 1.4 contains concluding remarks and also shows some stunningly accurate comparisons of the model and experiments.

## 1.2 Mathematical Model

Let the  $x$ -axis lie on the central axis of the fibre and be directed downwards in the direction of stretching (Fig. 1.1);  $y$  and  $z$  are then the transverse coordinates. At  $x = 0$  the cross-sectional geometry is that of the preform, which has cross-sectional area  $S_0$ , and at  $x = L$  the cross-sectional geometry is that of the fibre, which has cross-sectional area  $S_L$ , so that the neck-down region over which we model is  $0 \leq x \leq L$ . In this Eulerian reference frame fibre-drawing is a steady-state problem. Further, the effect of gravity is negligible. Then, for a preform of arbitrary geometry, we start with the full (3D) steady Navier–Stokes equations,

$$\begin{aligned}\nabla \cdot \mathbf{u} &= 0, \\ \rho(\mathbf{u} \cdot \nabla \mathbf{u}) &= -\nabla p + \nabla \cdot \boldsymbol{\sigma},\end{aligned}$$

where  $\mathbf{u} = (u, v, w)$  is the velocity vector,  $p$  is pressure,  $\boldsymbol{\sigma} = \mu(\nabla \mathbf{u} + (\nabla \mathbf{u})^T)$  is the usual viscous-stress tensor, and  $\rho$  and  $\mu$  are the constant density and temperature-dependent viscosity of the fluid. The fibre has a number of free-surface boundaries, the external free surface and the surfaces of each of the interior air channels. In this paper we denote the collection of free-surface boundaries by  $G(x, y, z, t) = 0$  on which we have the dynamic and kinematic boundary conditions

$$\boldsymbol{\sigma} \cdot \mathbf{n} = -\gamma \kappa \mathbf{n}, \quad \mathbf{u} \cdot \mathbf{n} = 0.$$

Here  $\gamma$  is the coefficient of surface tension, assumed to be constant,  $\kappa$  is the curvature of the boundary and  $\mathbf{n}$  is an outward normal to the boundary. In addition we have the boundary conditions

$$u(0, y, z) = U_0, \quad u(L, y, z) = U_L.$$

### 1.2.1 The Axial Stretching Problem

As discussed previously the geometry through the neck-down region from preform to fibre is slender so that we may, as is common [5, 7–9, 13, 15], use extensional flow theory. Thus we set  $\epsilon = \sqrt{S_0}/L \ll 1$  and then scale variables and parameters as follows:

$$\begin{aligned}\mu &= \bar{\mu}\mu^*, & \gamma &= \frac{\bar{\mu}U_0\sqrt{S_0}}{L}\gamma^*, \\ (x, y, z) &= L(x', \epsilon y', \epsilon z'), & p &= \frac{\bar{\mu}U_0}{L}p', \\ \mathbf{u} &= (u, v, w) = U_0(u', \epsilon v', \epsilon w'), & S &= S_0S',\end{aligned}$$

where primes denote dimensionless variables, asterisks denote dimensionless parameters, and  $\bar{\mu}$  is a typical viscosity. Because the resulting scaled equations involve only  $O(1)$  and  $O(\epsilon^2)$  terms, but no  $O(\epsilon)$  terms, we also expand scaled dependent variables in powers of  $\epsilon^2$  [7]:

$$\begin{aligned}u' &= u_0 + \epsilon^2 u_1 + \epsilon^4 u_2 + \dots, \\ v' &= v_0 + \epsilon^2 v_1 + \epsilon^4 v_2 + \dots,\end{aligned}$$

and so on. From this we find that, to leading order the axial velocity and pressure are independent of the transverse coordinates, i.e.  $u_0 = u_0(x, t)$  and  $p_0 = p_0(x, t)$ . As shown in [8], a similar process can be used to show that, at leading order, the temperature is independent of the transverse coordinates, so that this is also true of the temperature-dependent viscosity  $\mu$  and its scaled form  $\mu^*$ . In this paper we assume  $\mu(x)$  to be a known function and take  $\bar{\mu}$  to be its harmonic mean over the neck-down region,

$$\bar{\mu} = \frac{L}{\int_0^L 1/\mu(x)dx} \Rightarrow \int_0^1 \frac{1}{\mu^*(x')} dx' = 1.$$

Finally we note that the Reynolds number  $\text{Re} = \rho U_0 L / \bar{\mu}$  is much less than unity (typically  $\text{Re} \sim 10^{-8}$ ) so that inertia may be neglected.

With these scalings, and after considerable work [5, 7, 15], the leading-order model for  $S_0(x')$  and  $u_0(x')$  is obtained. Dropping primes on dimensionless variables and subscripts on the leading order components of the dependent variables, this is

$$u(x)S(x) = 1, \tag{1.1}$$

$$3\mu^*(x)Su_x + \frac{\gamma^*}{2}\sqrt{S}\Gamma = 6\sigma^*, \tag{1.2}$$

$$S(0) = 1, u(0) = 1, u(1) = D = 1/S(1), \tag{1.3}$$

where  $\Gamma(x)$  is the total length of all internal and external boundaries at position  $x$ ,  $\sigma^*$  is the scaled tension in the fibre, and  $D = U_L/U_0$  is the draw ratio. We refer to this as the axial stretching problem. Clearly, we may use (1.1) to substitute for  $u$  or  $S$  in (1.2), and so reduce this model to a single first-order ODE for  $S$  or  $u$ , with associated boundary conditions. We note that a given draw ratio  $D$  will dictate the fibre tension  $\sigma^*$  or vice versa. In general, we must determine  $\Gamma(x)$  from a model for the cross-plane flow but we first consider the case of zero surface tension  $\gamma^* = 0$

which removes the term involving  $\Gamma$  and enables straight-forward solution of the axial stretching problem.

### 1.2.2 The Case of Zero Surface Tension

This case was considered in detail by Dewynne and others [6, 7] who showed that, at leading order, the cross-plane flow solution may be written entirely in terms of the leading order axial flow component  $u$ ,

$$p = -\mu^* \frac{\partial u}{\partial x}, \quad v = -\frac{y}{2} \frac{\partial u}{\partial x}, \quad w = -\frac{z}{2} \frac{\partial u}{\partial x}.$$

From this solution we have that the cross section changes in *scale* but not in *shape*. Therefore, we need only solve for the cross-sectional area  $S(x)$  which has solution

$$S(x) = \exp\left(-2\sigma^* \int_0^x \frac{1}{\mu^*(x')} dx'\right),$$

$$S(1) = \frac{1}{D} = \exp(-2\sigma^*),$$

where we have made use of the fact that the harmonic mean of  $\mu^*$  over  $0 \leq x \leq 1$  is unity and found that the draw ratio  $D$  determines the fibre tension  $\sigma^*$ .

### 1.2.3 The Cross-Plane Flow Problem for Non-negligible Surface Tension

We now come to the leading order cross-plane flow problem for  $\gamma^* > 0$ . As shown by Cummings and Howell [5], the zero surface tension solution may be considered an eigensolution of this problem and the flow solution written as the sum of the eigensolution and a part due to surface tension. We also move to the reference frame moving with a cross-section from  $x = 0$  to  $x = 1$ , in which reference frame the problem is unsteady and the variable  $x$  is replaced by the time variable  $t$ . We rescale variables using the cross-sectional area  $S(x)$  as follows:

$$(y, z) = \sqrt{S}(\tilde{y}, \tilde{z}), \quad t = \tilde{t}, \quad \Gamma = \sqrt{S}\tilde{\Gamma}, \quad \kappa = \frac{\tilde{\kappa}}{\sqrt{S}}$$

$$p = p_{ZST} + \frac{\gamma^*}{\sqrt{S}}\tilde{p}, \quad (v, w) = (v_{ZST}, w_{ZST}) + \frac{\gamma^*}{\mu^*}(\tilde{v}, \tilde{w}),$$

where  $p_{ZST}$ ,  $v_{ZST}$ ,  $w_{ZST}$  is the leading order cross-plane flow solution for  $\gamma^* = 0$  and tildes denote the new dimensionless variables. In addition we use the ‘reduced time’ transformation introduced for constant viscosity in [5] and for temperature-dependent viscosity in [9],

$$\tau = \gamma^* \int_0^{\tilde{t}} \frac{dt}{\mu^* \sqrt{S}}.$$

The cross-plane problem so obtained is a classical 2D free-boundary Stokes-flow problem driven by unit surface tension in a domain of unit area:

$$\tilde{v}_{\tilde{y}} + \tilde{w}_{\tilde{z}} = 0, \quad \tilde{v}_{\tilde{y}\tilde{y}} + \tilde{v}_{\tilde{z}\tilde{z}} = \tilde{p}_{\tilde{y}}, \quad \tilde{w}_{\tilde{y}\tilde{y}} + \tilde{w}_{\tilde{z}\tilde{z}} = \tilde{p}_{\tilde{z}}, \quad (1.4)$$

$$G_{\tilde{\tau}} + \tilde{v}G_{\tilde{y}} + \tilde{w}G_{\tilde{z}} = 0, \quad \text{on } G = 0, \quad (1.5)$$

$$G_{\tilde{y}}(-\tilde{p} + 2\tilde{v}_{\tilde{y}}) + G_{\tilde{z}}(\tilde{v}_{\tilde{z}} + \tilde{w}_{\tilde{y}}) = -\tilde{\kappa}G_{\tilde{y}}, \quad \text{on } G = 0, \quad (1.6)$$

$$G_{\tilde{y}}(\tilde{v}_{\tilde{z}} + \tilde{w}_{\tilde{y}}) + G_{\tilde{z}}(-\tilde{p} + 2\tilde{w}_{\tilde{z}}) = -\tilde{\kappa}G_{\tilde{z}}, \quad \text{on } G = 0, \quad (1.7)$$

Here subscripts denote differentiation with respect to the subscript variable. Solution of the cross-plane problem gives the re-scaled cross-flow and cross-sectional geometry, including the boundary length  $\tilde{\Gamma}$ , as functions of reduced time  $\tau$ .

### 1.2.4 Coupling of Axial Stretching and Cross-Plane Flow Problems

The cross-plane problem (1.4)–(1.7) in terms of  $\tau$  is coupled with the Eulerian axial stretching problem (1.1)–(1.3) in terms of  $x$  via

$$\frac{dx}{d\tilde{t}} = u \quad \Rightarrow \quad \frac{\gamma^*}{\mu^* \sqrt{S}} \frac{dx}{d\tau} = u, \quad x(0) = 0. \quad (1.8)$$

While a solution has been obtained for a thin-walled tube with  $\mu^*$  an exponential function of temperature [9], obtaining a solution more generally is difficult. However, as shown by Stokes et al. [15] the two coupled problems are readily solved for general geometries and viscosity functions if the 1D axial stretching model is written in terms of the variable  $\tau$ ,

$$-\frac{3\gamma^*}{\sqrt{S}} \frac{dS}{d\tau} + \frac{\gamma^*}{2} \Gamma(\tau) = 6\sigma^*,$$

and putting  $\chi = \sqrt{S}$  and  $\Gamma = \sqrt{S}\tilde{\Gamma}$  reduces this to the first-order ODE

$$\frac{d\chi}{d\tau} - \frac{\chi}{12} \tilde{\Gamma} = -\frac{\sigma^*}{\gamma^*},$$

where  $\tilde{\Gamma}(\tau)$  is obtained from the cross-plane problem which is independent of the axial stretching problem and may be solved first. Defining the integrating factor

$$H(\tau) = \exp\left(-\frac{1}{12} \int_0^\tau \tilde{\Gamma}(\tau') d\tau'\right), \quad (1.9)$$

the solution may be written as

$$\chi(\tau) = \frac{1}{H(\tau)} \left(1 - \frac{\sigma^*}{\gamma^*} \int_0^\tau H(\tau') d\tau'\right). \quad (1.10)$$

Thus, in summary, the cross-plane model gives the total boundary length  $\tilde{\Gamma}(\tau)$ ,  $0 \leq \tau \leq \tau_1$  where  $\tau_1$  determines the fibre shape but not its size. Any appropriate analytical or numerical method may be used to solve for the cross-plane shape and boundary length and, hence for the integrating factor (1.9). The stretching flow problem has the exact solution (1.10) in terms of the integrating factor. The draw ratio  $D = U_L/U_0 = 1/\chi^2(\tau_1) = 1/S(\tau_1)$  determines the size of the final fibre cross-section and, from (1.10), we have the relation between the fibre shape ( $\tau_1$ ) and the ratio of fibre and surface tension ( $\sigma^*/\gamma^*$ ),

$$\frac{1}{\sqrt{D}} = \frac{1}{H(\tau_1)} \left(1 - \frac{\sigma^*}{\gamma^*} \int_0^{\tau_1} H(\tau') d\tau'\right).$$

From (1.8) we obtain the separable ODE relating  $\tau$  and  $x$ ,

$$\frac{dx}{d\tau} = \frac{\mu^*}{\gamma^* \chi}, \quad x(0) = 0,$$

integration of which gives the fibre tension  $\sigma^*$ ,

$$\int_0^1 \frac{1}{\mu^*(x')} dx' = 1 = -\frac{1}{\sigma^*} \log\left(\frac{H(\tau_1)}{\sqrt{D}}\right).$$

The model involves the four parameters  $\sigma^*$  (fibre tension),  $\gamma^*$  (surface tension),  $D = U_L/U_0 = S_0/S_L$  (draw ratio, equivalently fibre size), and  $\tau_1$  (fibre geometry). These are not all independent; two must be specified and the remaining two determined as part of the solution.

An important result from this solution is that for drawing a desired fibre from a given preform we can use the model to determine the required physical fibre tension without knowing the temperature profile. As discussed in detail in [15], for a given preform geometry and a given fibre geometry (i.e.  $D$  and  $\tau_1$ ), the model gives the required ratio  $\sigma^*/\gamma^*$  which is related to the ratio of the physical parameters  $\sigma$  and  $\gamma$  by

$$\frac{\sigma^*}{\gamma^*} = \frac{1}{6\sqrt{S_0}} \frac{\sigma}{\gamma}. \quad (1.11)$$

Since the surface tension  $\gamma$  is a known fluid property and the cross-sectional area  $S_0$  of the preform is also known, we may use (1.11) to compute the physical fibre tension  $\sigma$ . Provided the draw tower allows for measurement of fibre tension during a draw, the furnace temperature can be adjusted to achieve the desired fibre tension without the need to know anything about the fluid temperature itself. In fact, since the model also gives  $\sigma^*$  and assuming the (approximate) neck-down length is known, the (approximate) harmonic mean of the fluid temperature through the neck-down region may be computed from

$$\sigma = \frac{\bar{\mu} U_0 S_0}{L} 6\sigma^* \Rightarrow \bar{\mu} = \frac{\sigma L}{6U_0 S_0 \sigma^*}.$$

### 1.3 Forward and Inverse Solutions

Solution of the forward problem is done by solving the cross-plane problem for a given preform geometry over reduced time  $0 \leq \tau \leq \tau_1$ , for some chosen value  $\tau_1$ , and then solving the axial stretching problem. Solution of the inverse problem is achieved by solving the cross-plane problem backwards from a given fibre geometry. When the cross-plane problem may be solved analytically, both forward and inverse problems are easily solved; see, for example, the solutions given in [15] for the drawing of (i) an annular tube and (ii) the tube made by arranging a number of circular rods of appropriate radius in a circle. These two examples were also used to show that the inverse problem is inherently unstable; small imperfections in the description of the fibre are amplified as the model is run backwards, leading to different preform geometries, some of which may not be practical.

To overcome this instability in numerical solution of the inverse cross-plane problem, some form of regularisation must be used. An example of this is [1] where a modified form of Crowdy's [4] elliptical-pore model, which constrains elliptical holes in the 2D cross-section to remain elliptical as they evolve, is obtained and used to solve both forward and inverse problems. Figure 1.3, reproduced from [1], shows some different preform cross-sectional geometries each of which will yield the same fibre geometry when drawn using the correct value of the draw ratio and fibre tension.

### 1.4 Conclusions

In this paper we have reviewed the development of an efficient mathematical model for fibre drawing using extensional flow theory. The model is comprised of a 2D free-boundary Stokes-flow problem describing the flow and geometry evolution in the

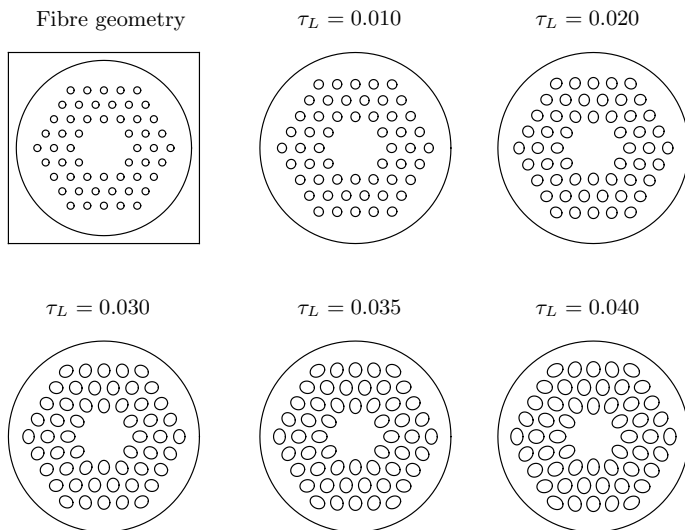


**Fig. 1.3** Options for preform geometries yielding the fibre geometry shown, calculated by running the elliptical-pore model backwards. To obtain a fibre with the geometry shown and a given cross-sectional area the preform of chosen geometry must be drawn with the correct draw ratio and the correct fibre tension which may be determined from the model solution. © 2015 Cambridge University Press, Reprinted with permission from Buchak et al., *J. Fluid Mech.* 778, 5–38 [1, fig. 14]

cross-section, and a 1D axial stretching problem which describes the change in cross-sectional area from preform to fibre. By writing and solving both of these problems in a reference frame moving with a cross-section, and in terms of an appropriately transformed time variable, an analytic solution of the axial stretching problem for the evolution of the cross-sectional area has been obtained in terms of a function involving the total boundary length of the cross-section. This boundary length must be obtained by solving the 2D cross-plane problem; for some geometries analytical solutions are available but, in general, the 2D cross-plane problem must be solved numerically. This model is applicable to fibres of arbitrary cross-sectional geometry and it enables solution of both forward and inverse problems. When solving the inverse problem the cross-plane problem is run in reverse and some form of regularisation may be needed to overcome instability and ensure practically realisable preform geometries.

It is noteworthy that the model enables determination of the tension in the fibre required to draw a given fibre from a given preform, without the need to know anything about the temperature of the fibre material. Then, when using a draw tower fitted with a tension-measuring device, the furnace temperature can be adjusted to yield the required fibre tension. This is of great practical value since determining the temperature and, therefore, the viscosity, through the neck-down region is extremely difficult, if not impossible. We also here note that the model indicates that all temperature profiles which yield viscosity profiles with the same harmonic mean through the neck-down region give the same fibre from a given preform. The temperature

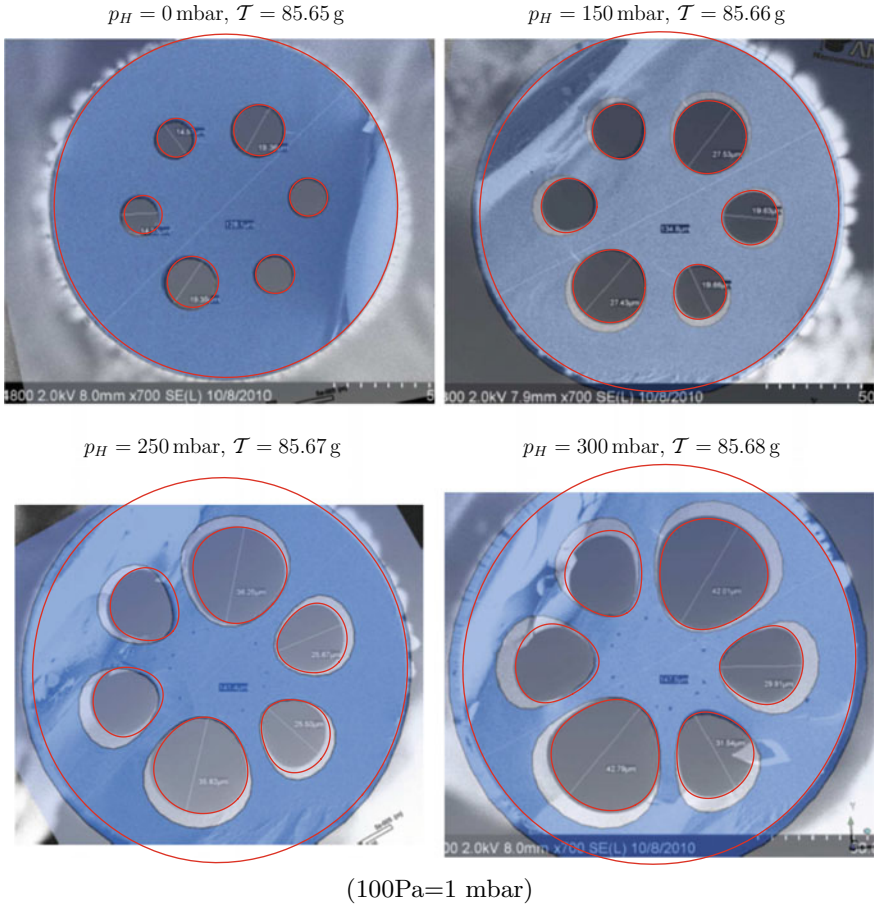


**Fig. 1.4** Experimental microscope images of the fibre cross-section, overlaid with the finite element simulation of [12] (pale blue transparency) and the results of the new asymptotic simulation (thin red lines). Shown are the four values of pressurisation from [12, Fig. 3]. For each example the pressurisation applied is shown in the caption above the image, along with the fibre tension as calculated by the iterative scheme. © 2016 IEEE. Reprinted, with permission, from Chen et al., J. Lightwave Tech. 34(24), 5651–5656 [3, Fig. 4]

profile affects the evolution of the geometry along the neck-down region but not the end result.

Although not discussed in this paper, it is possible to include active pressurisation of the air channels during fibre drawing, which modifies the balance between fibre tension and surface tension. In this case there is two-way coupling between the cross-plane flow and axial stretching problems which must be solved simultaneously. Importantly, measurement of fibre tension still circumvents the need to know the temperature profile. For further detail on this model see [2].

Figure 1.4, taken from [3], compares the extensional-flow model including active pressurisation with experimental results and a 3D finite-element simulation for a 6-hole preform with an external diameter of 4 mm. The extensional-flow model captures the cross-sectional fibre geometry extremely well and better than the finite-element simulation. This provides excellent validation of the extensional-flow modelling approach. For further details see [3].

In closing we note that the model accuracy decreases as the preform diameter and the draw ratio increase. Good comparison is seen between model and experiment for preforms with external diameters up to around 10 mm and the model is a useful predictive tool for determining how to fabricate a desired fibre. For quite large preform diameter, around 3 cm, there is reasonable qualitative agreement between model and experiment for some choices of parameters but significant discrepancy for others, in particular large draw ratio and large tension. This is the subject of ongoing research.

## References

1. Buchak, P., Crowdy, D.G., Stokes, Y.M., Ebendorff-Heidepriem, H.: Elliptical pore regularisation of the inverse problem for microstructured optical fibre fabrication. *J. Fluid Mech.* **778**, 5–38 (2015). <https://doi.org/10.1017/jfm.2015.337>
2. Chen, M.J., Stokes, Y.M., Buchak, P., Crowdy, D.G., Ebendorff-Heidepriem, H.: Microstructured optical fibre drawing with active channel pressurisation. *J. Fluid Mech.* **783**, 137–165 (2015). <https://doi.org/10.1017/jfm.2015.570>
3. Chen, M.J., Stokes, Y.M., Buchak, P., Crowdy, D.G., Ebendorff-Heidepriem, H.: Asymptotic modelling of a six-hole MOF. *J. Lightwave Tech.* **34**, 5651–5656 (2016). <https://doi.org/10.1109/JLT.2016.2628438>
4. Crowdy, D.G.: An elliptical-pore model of late-stage planar viscous sintering. *J. Fluid Mech.* **501**, 251–277 (2004). <https://doi.org/10.1017/S0022112003007559>
5. Cummings, L.J., Howell, P.D.: On the evolution of non-axisymmetric viscous fibres with surface tension, inertia and gravity. *J. Fluid Mech.* **389**, 361–389 (1999). <https://doi.org/10.1017/S0022112099005030>
6. Dewynne, J.N., Ockendon, J.R., Wilmott, P.: A systematic derivation of the leading-order equations for extensional flows in slender geometries. *J. Fluid Mech.* **244**, 323–338 (1992). <https://doi.org/10.1017/S0022112092003094>
7. Dewynne, J.N., Howell, P.D., Wilmott, P.: Slender viscous fibres with inertia and gravity. *Q. J. Mech. Appl. Math.* **47**, 541–555 (1994). <https://doi.org/10.1093/qjmam/47.4.541>
8. Fitt, A.D., Furusawa, K., Monroe, T.M., Please, C.P., Richardson, D.A.: The mathematical modelling of capillary drawing for holey fibre manufacture. *J. Eng. Maths* **43**, 201–227 (2002). <https://doi.org/10.1023/A:1020328606157>
9. Griffiths, I.M., Howell, P.D.: Mathematical modelling of non-axisymmetric capillary tube drawing. *J. Fluid Mech.* **605**, 181–206 (2008). <https://doi.org/10.1017/S002211200800147X>
10. Institute for Photonics and Advanced Sensing: Research themes (2017). <https://www.adelaide.edu.au/ipas/research/>, viewed 19 November 2017
11. Knight, J.C.: Photonic crystal fibres. *Nature* **424**, 847–851 (2003). <https://doi.org/10.1038/nature01940>
12. Luzzi, G., Eppele, P., Scharrer, M., Fujimoto, K., Rauh, C., Delgado, A.: Numerical solution and experimental validation of the drawing process of six-hole optical fibers including the effects of inner pressure and surface tension. *J. Lightwave Technol.* **30**, 1306–1311 (2012). <https://doi.org/10.1109/JLT.2012.2185486>

13. Matovich, M.A., Pearson, J.R.A.: Spinning a molten threadline; steady-state isothermal viscous flows. *Ind. Eng. Chem. Fund.* **8**, 512–520 (1969). <https://doi.org/10.1021/i160031a023>
14. Pearson, J.R.A., Petrie, C.J.S.: The flow of a tubular film. Part 2 Interpretation of the model and discussion of solutions. *J. Fluid Mech.* **42**, 609–625 (1970). <https://doi.org/10.1017/S0022112070001507>
15. Stokes, Y.M., Buchak, P., Crowdy, D.G., Ebdorff-Heidepriem, H.: Drawing of microstructured fibres: circular and noncircular tubes. *J. Fluid Mech.* **755**, 176–203 (2014). <https://doi.org/10.1017/jfm.2014.408>
16. Xue, S.C., Tanner, R.I., Barton, G.W., Lwin, R., Large, M.C.J., Poladian, L.: Fabrication of microstructured optical fibres - part I: problem formulation and numerical modelling of transient draw process. *J. Lightwave Technol.* **23**, 2245–2254 (2015). <https://doi.org/10.1109/JLT.2005.850055>
17. Xue, S.C., Tanner, R.I., Barton, G.W., Lwin, R., Large, M.C.J., Poladian, L.: Fabrication of microstructured optical fibres - part II: numerical modelling of steady-state draw process. *J. Lightwave Technol.* **23**, 2255–2266 (2015). <https://doi.org/10.1109/JLT.2005.850058>
18. Yarin, A.L.: Surface-tension-driven flows at low Reynolds number arising in optoelectronic technology. *J. Fluid Mech.* **286**, 173–200 (1995). <https://doi.org/10.1017/S0022112095000693>

# Chapter 2

## A Numerical Study on Free Hovering Fruit-Fly with Flexible Wings



Y. Yao, K. S. Yeo and T. T. Nguyen

**Abstract** Insect flyers have drawn the attention of many biologists, mechanists and engineers due to their unparalleled manoeuvrability. In this article, we introduce a comprehensive FSI model to investigate a model fruit-fly with flexible wings. We then apply the model in the numerical study of the interaction between aerodynamic and structural processes in free hovering flight. The model fruit-fly is allowed to fly with six-degrees of freedom (6-DoF) and hovers steadily with active wing kinematic control. The present study provides a convenient approach to track the dynamic deformation of flexible wings and the instantaneous aerodynamic forces and power in free flight. The results of hovering flight simulations show that the flexibility of insect wing allows the wing to bend and passively adapt to the detaching direction of leading-edge vortices (LEVs), which helps to enhance lift force and reduce the aerodynamic power consumption in free flight.

**Keywords** Insect flight · Flexible wing · Free flight · Computational fluid dynamics · Fluid-structure interaction

### 2.1 Introduction

Winged insects are amazingly agile flapping wing flyers which can hover, fly upside down, and execute rapid manoeuvres [1]. The flapping wing flights are more efficient in low Reynolds number regime, which outperforms conventional fixed and rotary wing aircrafts [2]. Due to their unparalleled manoeuvrability and efficiency, winged insects have long captured the interest of zoologists and aerodynamicists. The advance of computational fluid dynamics (CFD) enabled researchers to explore the unsteady aerodynamics of flapping wings and behaviours of free insect flight via numerical approaches. The aerodynamic performance of insect flight in different scenarios has been investigated in the literature [2–4]. Moreover, there have been also

---

Y. Yao (✉) · K. S. Yeo · T. T. Nguyen  
National University of Singapore, 9 Engineering Drive 1, Singapore 117575, Singapore  
e-mail: [yaoyang@u.nus.edu](mailto:yaoyang@u.nus.edu)

© Springer Nature Switzerland AG 2019  
S. Gutschmidt et al. (eds.), *IUTAM Symposium on Recent Advances in Moving Boundary Problems in Mechanics*, IUTAM Bookseries 34,  
[https://doi.org/10.1007/978-3-030-13720-5\\_2](https://doi.org/10.1007/978-3-030-13720-5_2)

several attempts to model natural flexible insect wings via fluid-structural interaction (FSI) analysis [5, 6]. The recent work of Nguyen et al. [6] enabled the modelling of flexible wings with large deformation and revealed that wing flexibility plays an important role in allowing insect wings to undergo aerodynamically favourable deformation. However, few studies integrated the deformation of wing in free insect flight study. Thus, the effects of wing flexibility on natural free flight remain untouched.

In this article, we present a comprehensive FSI model for insect flight with flexible wings and set out to seek for a better understanding of the interaction between aerodynamic and structural processes in free flights. The model insect is allowed to fly with six-degrees of freedom (6-DoF) and comprises a pair of flexible wings. The present numerical method allows the interaction between meshfree node cloud surrounding moving bodies and background Cartesian grid, and will be described in Sect. 2. In Sect. 3, the flight performances of model insects with rigid and flexible wings are presented and analysed respectively. Some qualitative aspects of the fluid dynamics are discussed to provide insights in the effect of flexibility on aerodynamic loads on the flapping wings. The key conclusions arising from the present work are summarized in Sect. 4.

## 2.2 Methods

### 2.2.1 Modelling of Free Flying Insect

To correctly simulate insect motion in free flight, flow field surrounding flying insect needs to be solved to evaluate unsteady aerodynamic forces generated by flapping wings. The complex geometry and dynamics of the flyer make simulation of such flows highly challenging for conventional computational fluid dynamics (CFD) methods. In this study, we solve moving boundary problem involved in flapping wing flight with a singular value decomposition (SVD) based generalized finite difference (GFD) scheme on a hybrid coupled Cartesian-meshfree grid system. The SVD-GFD method was first proposed by Ang et al. [7], then was further extended to solve complex moving boundary problems like insect flapping flight, fish swimming, and others. The present methodology has been validated by comparing results obtained in standard cases with numerical and experimental data published in the literature.

The computational setup used for ground effect study is presented in Fig. 2.1. The flow field between the wing stroke plane and the ground was discretized by uniform Cartesian mesh (grid interval  $0.025R$ , and  $R$  is the wing length of the flyer) to obtain satisfactory resolution. Highly refined meshfree grid was used near the surfaces as shown in Fig. 2.1b.

The motion of the flyer is driven by the reaction force of the fluid obtained in the numerical simulation. Once the flow field is solved by the aforementioned numerical methods, aerodynamic forces can be computed to obtain the solution of the kinematic and dynamics equations in accordance with Newton's laws.

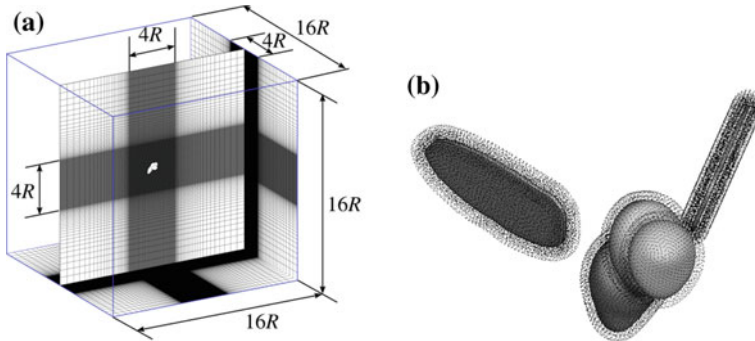


**Fig. 2.1** Configuration of computational grid for free hovering fruit-fly study. **a** Background Cartesian mesh; **b** Meshfree cloud around the model insect

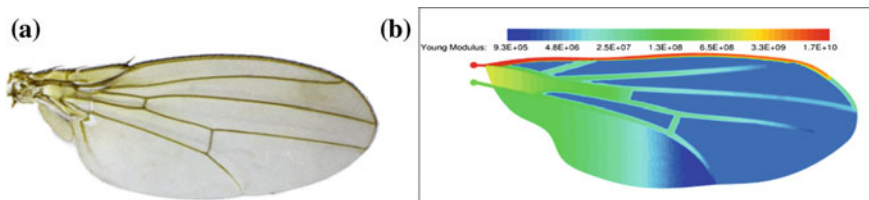


**Fig. 2.2** Insect wing model adapted from Nguyen et al. [6]. **a** Natural fruit-fly wing; **b** LER wing model

### 2.2.2 Modelling of Flexible Wing

The non-linear dynamics of the flexible wings under coupled inertia-aerodynamic loadings is then modelled through a finite element method-based loose fluid-structural coupling process described in [6]. The open-source FEA library, Vega [8], which offers a wide choice of numerical schemes and material models, was adopted this study to solve the non-linear structural dynamic problems related to flexible wings.

The discretized second order system of differential equations that describes the motion of a deformable solid can be constructed using the principle of virtual work and finite element discretization [9]. The co-rotational linear elasticity model is chosen thanks to its relative simplicity, inexpensive computational cost and good behaviour in problems involving large deformation [8]. The implicit Newmark integrator is selected to advance the solution in time due to its reliability [10].

A leading-edge reinforced (LER) wing shown in Fig. 2.2 is adopted in this work to better represent the thin shell structures of natural flexible wings. The LER wing features a distribution of stiffening veins and connecting soft membrane that is abstracted from that of the natural wing. The construction and properties of the LER wing may be found in [6] with details.

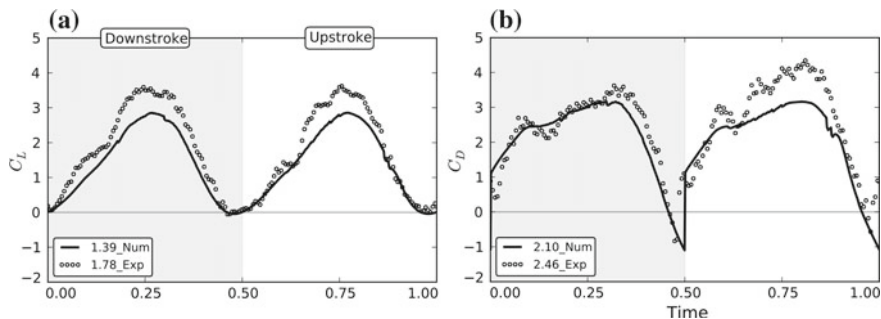


**Fig. 2.3** Instantaneous lift and drag histories of a fruit-fly wing executing simple harmonic motion at  $Re = 200$

### 2.2.3 Validation

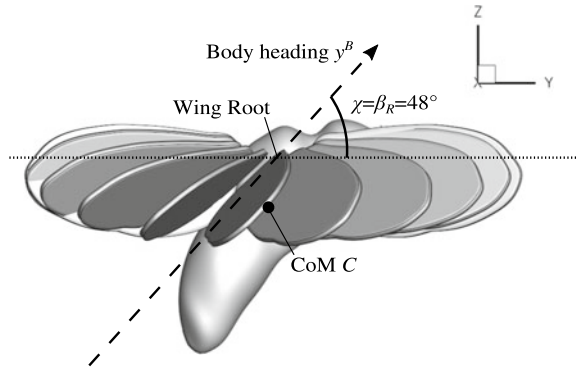
We adopted the experimental results in Lua et al. [11] to validate the CFD scheme presented in this paper. In the experiments of Lua et al., the forces on the insect wings were estimated from a scaled robot wing and normalized to the insect scale. As shown in Fig. 2.3, our numerical results closely tracked the build-up and decrease of the experimental data, and correctly captured major force peaks and troughs in the whole wingbeat. This relative error between experimental and numerical results also agreed with the previous numerical studies [4, 12], and it may be caused by the oscillation/flutter of the robotic wing due to its imperfect rigidity and slips within the actuator mechanisms. The general agreement indicates that the present FSI solver can predict the force generation of insect wings with sufficient accuracy for our purpose. More comprehensive validations for the FSI solver, including analyses of non-deformable, stationary and moving objects, can be found in the authors' previous paper [6].

## 2.3 Results and Discussions

Many insects have been observed to hover with approximately horizontal stroke plane [13]. This flight status is named normal hovering, and has been considered as the most basic mode of flapping wing flight by researchers [4, 14]. In the present work, we implement the proposed FSI model to investigate the effects of wing flexibility on the normal hovering flight of a model fruit-fly.

The morphological model of the fruit-fly was extracted from the images photographed by Fry et al. [14] and Holtzman and Kaufman [15]. The model flyer has a wing length of  $R = 2.39$  mm and a body length of  $L = 2.78$  mm. The basic wing kinematics was assumed to be simple harmonic motion with an initial flapping fre-

**Fig. 2.4** Designated body posture in normal hovering flight



quency of  $f = 260$  Hz. Then the Reynolds number of the flapping wing flight, which represent the ratio of inertial to viscous aerodynamic forces, could be determined:

$$\text{Re}_{flap} = \frac{\Phi f R^2}{\nu}$$

where  $\Phi$  is the stroke amplitude and  $\nu$  is viscosity. A nominal Re of 148 may be worked out for Fry et al.'s sample of six free hovering fruit flies [14], which had an average wing-beat frequency  $f = 218$  Hz (range 211–227 Hz).

The flyer was controlled to maintain a designated posture shown in Fig. 2.4. In normal hovering flight, the mean body angle  $\bar{\chi}$  was set to  $48^\circ$ , while the stroke-plane was set to be horizontal at the non-dimensional time  $t^* = 0$ . In the simulations, the model flyer is regulated by a stroke-plane based kinematic control algorithm to maintain long-term steady hovering status. The basic wing kinematics was assumed to be simple harmonic motion with an initial flapping frequency of 260 Hz. The stroke-plane was adjusted forward or backward within a set range of  $\beta_R = \beta_{R,0} \pm 6^\circ$ , where  $\beta_R$  is the angle between stroke-plane and body heading, to keep the flyer stay at the designated position. A small stroke bias was then set and adjusted actively in the flight to keep the net pitch moment in balance.

### 2.3.1 Flight Performance

Figures 2.5 and 2.6 show the details of the flyer's motion in normal hovering over a period of 100 wingbeats with rigid and flexible wings respectively. The body displacement was normalized by the wing length  $R$ . The time histories of body displacement and rotation presented in Figs. 2.5 and 2.6 indicate that the lateral motion (yawing, rolling and lateral displacement ( $x$ -direction)) is negligible in hovering flight. There was a significant body oscillation appearing in the first ten wingbeats of the hovering flight ( $t^* < 10$ ). The flyer then gradually stabilized to steady cyclical motion in the

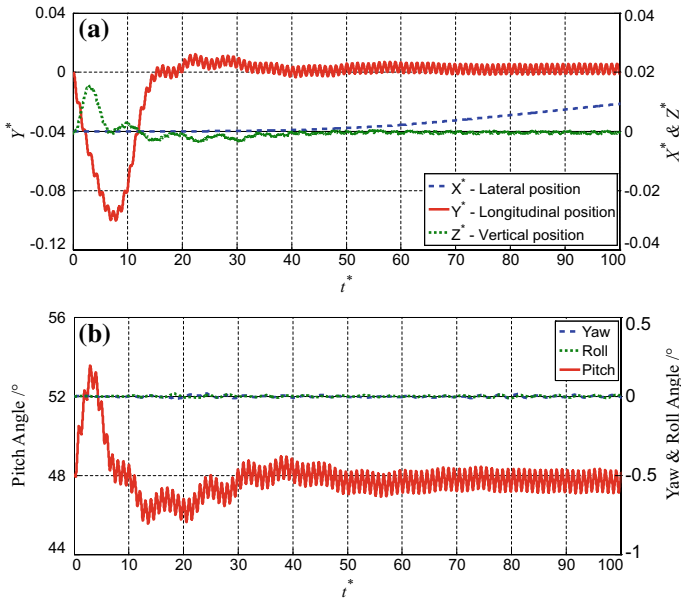


**Fig. 2.5** Time histories of motion and kinematic parameters in normal hovering flight with rigid wings. **a** Displacement of centre of mass; **b** Yaw, roll and pitch angles of the flyer

course of simulation. The rigid wing flyer deviated about  $0.1R$  backward,  $0.015R$  upward from the designated hovering position in the early stage of flight (Fig. 2.5a), while the body pitched up about  $5.5^\circ$  (Fig. 2.5b). For the flexible wing flyer, the maximum deviation of the body displacement was about  $0.052R$  backward,  $0.018R$  upward (Fig. 2.6a), and it was about  $2.7^\circ$  for body pitch (Fig. 2.6b).

The large body oscillation at the beginning of flight is due to the unbalanced forces and moments produced in the first wingbeat as the flyer accelerate its flapping wings from rest. The decreased deviation in the flexible wing flight indicates the deformation of the LER wings would reduce the unbalanced pitch moment and longitudinal force in the 1st wingbeat compared with the rigid wing. The smaller pitch angle further alleviated the burden of the horizontal motion control. This alleviated initial body oscillation leads to a 20% cut-down of the settling time in the flight with flexible LER wings (see Table 2.1).

Moreover, comparing the results shown in Table 2.1, it is noted that the steady-state body fluctuations associated with wing flapping slightly decreased on the flight with flexible wings. The 10-wingbeat mean flapping frequency also reduced in the flexible wing case. We further computed the peak and 10-wingbeat mean power consumption in steady hovering flight. The results provided in Table 2.1 agree well with experimental data in [14]. The different power consumptions indicate that the flexible wing flight is more efficient than the rigid wing one. The mean power consumption of the flexible wing flight was about 20% less than that of the rigid wing flight. The